



Available online at www.sciencedirect.com

ScienceDirect



Nuclear Physics A 1021 (2022) 122424

www.elsevier.com/locate/nuclphysa

Excitation function of 54 Fe(p, α) 51 Mn from 9.5 MeV to 18 MeV

Wilson Lin ^{a,*}, John T. Wilkinson ^b, Kendall E. Barrett ^a, Todd E. Barnhart ^a, Matthew Gott ^c, Kaelyn V. Becker ^a, Adam M. Clark ^b, Anthony Miller ^b, Gunnar Brown ^b, Molly DeLuca ^b, Robert Bartsch ^b, Graham F. Peaslee ^b, Jonathan W. Engle ^{a,d}

Received 5 January 2022; received in revised form 17 February 2022; accepted 18 February 2022 Available online 25 February 2022

Abstract

Excitation function of the 54 Fe(p, α) 51 Mn reaction was measured from 9.5 to 18 MeV E_{0,p^+} by activating a foil stack of 54 Fe electrodeposited on copper substrates. Residual radionuclides were quantified by HPGe gamma ray spectrometry. Both 51 Mn ($t_{1/2}=46.2$ min, $\langle E_{\beta^+}\rangle=963.7$ keV, $I_{\beta^+}=97\%$; $E_{\gamma}=749.1$ keV, $I_{\gamma}=0.265\%$) and its radioactive daughter, 51 Cr ($t_{1/2}=27.704$ d, $E_{\gamma}=320.1$ keV, $I_{\gamma}=9.91\%$), were used to indirectly quantify formation of 51 Mn. Results agree within uncertainty to the only other measurement in literature and predictions of default TALYS theoretical code. Final relative uncertainties are within $\pm 12\%$. © 2022 Elsevier B.V. All rights reserved.

Keywords: Excitation function; Gamma spectroscopy; Gamma spectrometry; Tandem Van de Graaff accelerator; Manganese-51; Positron emission tomography

E-mail address: wlin99@wisc.edu (W. Lin).

Department of Medical Physics, University of Wisconsin, 1111 Highland Ave., Madison, WI, 53705, United States
 Department of Physics, University of Notre Dame, Notre Dame, IN, 46556, United States

^c Physics Division, Argonne National Laboratory, 9700 South Cass Avenue, Lemont, IL, 60439, United States

d Department of Radiology, University of Wisconsin, 600 Highland Ave., Madison, WI, 53792, United States

^{*} Corresponding author.

1. Introduction

 51 Mn ($t_{1/2} = 46.2$ min, $< E_{\beta^+} >= 963.7$ keV, $I_{\beta^+} = 97\%$; $E_{\gamma} = 749.1$ keV, $I_{\gamma} = 0.265\%$) is a short-lived radionuclide currently being investigated as a potential positron emission tomography (PET) tracer for pancreatic imaging (see [1,2] and references therein). 51 Mn has been made by small cyclotrons via 50 Cr(d,n) 51 Mn [1], but established techniques for 54 Fe target recycling make 54 Fe(p, α) 51 Mn more attractive. Only a single measurement of the 54 Fe(p, α) 51 Mn excitation function has been reported [3], whereas two measurements of 50 Cr(d,n) 51 Mn have been reported [4,5].

We measured the 54 Fe(p, α) 51 Mn excitation function on the 11MV FN Tandem Van de Graaff accelerator at University of Notre Dame's (ND) Nuclear Science Laboratory (NSL) with proton energies (E_{0,p^+}) up to 18 MeV and collimated beam widths less than 5 mm. Although $E_{0,p^+}=18$ MeV is below the predicted maximum of the 54 Fe(p, α) 51 Mn cross section, it is representative of many commercial cyclotrons [6]. We quantified residuals with ND's on-site high purity germanium detector (HPGe), and corroborated ND spectra with HPGe measurements at University of Wisconsin-Madison (UWM).

We present an experimentally determined excitation function of 54 Fe(p, α) 51 Mn from 9.5 MeV to 18 MeV and discuss clinical relevance based on our results. The measured cross sections include uncertainties in absolute detector efficiency, beam current, counting statistics, number of 54 Fe atoms and FN tandem characteristics.

2. Materials and methods

2.1. ⁵⁴Fe target fabrication and irradiation

Aqueous solutions were made from $> 18 \text{ M}\Omega/\text{cm H}_2\text{O}$. Targets were prepared by electrolytic deposition of isotopically enriched ⁵⁴Fe metal (99.7% ⁵⁴Fe, 0.28% ⁵⁶Fe, 0.01% ⁵⁷Fe, 0.01% ⁵⁸Fe; ISOFLEX) on natural copper substrates (99.8% purity, nominally 10 μm from (Alfa Aesar), in a similar process previously described in [7]. Due to time constraints at ND, and to provide an alternative measure of beam parameters, copper was selected as the backing material to allow simultaneous determination of beam energy and current when assaying ⁵¹Mn and ⁵¹Cr by using $^{\text{nat}}$ Cu(p,x) 6x Zn monitor reactions. Copper substrates were cut into squares of approximately 1.5 × 1.5 cm² and weighed on a calibrated digital scale with sub-milligram precision. The relative uncertainty in the areal density of ^{nat}Cu foils was less than 4%. 50-70 mg of ⁵⁴Fe metallic powder was dissolved in 1 mL 6 M HCl (concentrated HCl from Fisher Chemical) and 100 ul of 30% H₂O₂ (Fisher Chemical). Upon complete dissolution, 10 mL of saturated (NH₄)₂C₂O₄ (Alfa Aesar) was added. The electrolyte was then buffered to pH = 4 using 28% NH₄OH (Sigma-Aldrich) and/or 6 M HCl and transferred to a cylindrical plating cell. A platinized titanium mesh anode was positioned approximately 2 cm above the copper substrate and a potential of 3.0 \pm 0.2 V was applied, corresponding to an initial current of 19 ± 3 mA. The electroplated region had a diameter of 9.0 ± 0.2 mm (average area 0.64 cm², Fig. 1A), and electrodeposition lasted 1-2 h. Targets were rinsed with ethanol, dried, and weighed (N = 3) to determine the plated ⁵⁴Fe mass, where all measurements were repeatable within ± 0.3 mg.

Targets were irradiated with $E_{0,p^+} = 9.5$ MeV-18 MeV, where an analyzing magnet filtered incident beam energies to within ± 30 keV of the setpoint. The analyzing magnet was tuned with deuteron magnetic resonance using a sample of [2 H]H $_2$ O. The generating voltmeter, along with a slit control feedback using the beam, helped to monitor the voltage setpoint. Calculated beam

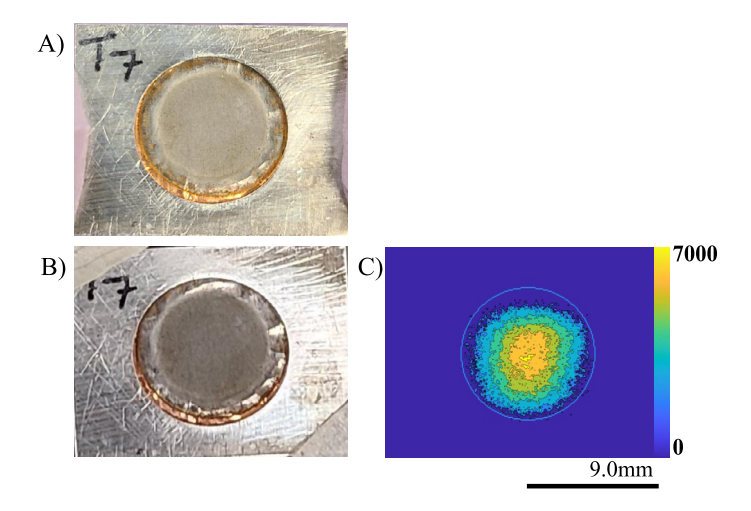


Fig. 1. A) Example sample target mounted on the aluminum frame for irradiation. The iron thickness was $9.5 \pm 0.8 \,\mu m$. B) Target after irradiation. C) Activation profile of the same target, the circular outline depicts a 9 mm diameter circle. The intensity is linearly correlated with activity at these levels.

energies from ^{6x}Zn products agreed within uncertainty to expected setpoint energies. A titanium hydride cathode served as the source of protons from the Source of Negative Ions by Cesium Sputtering (SNICS) ion source. Beam current was measured on an electrically isolated station connected to the target holder and the beam dump. An external magnetic field was applied to this irradiation line to geometrically suppress leakage of recoil electrons. More information regarding the accelerator can be found in [8–10], where a schematic of the beam setup is provided.

A small correction based on SRIM calculations was applied to the beam energy incident on the copper foils due to interactions with ⁵⁴Fe (total average energy loss of 140-240 keV per ⁵⁴Fe target). Energies reported for each target were calculated at the midpoint of the material. After irradiation with beam currents of 145-300 nA, ranging from fifteen minutes to an hour, the plated ⁵⁴Fe targets showed no changes in appearance and were well-adhered to the copper backing (see Fig. 1B). Following irradiation, the targets were left on the sample holder for approximately one hour to reduce exposure to personnel. Then, the samples were transported to the low-background counting station within the NSL with a Canberra model GC3518 HPGe and a sample storage area for assaying. The HPGe at ND was surrounded by lead shielding, with the longitudinal axis free for sample placement. After preliminary data were acquired at ND, samples were shipped to UWM for further assay on a different detector (Canberra C1519 HPGe). The detector setup at UWM was shielded on two sides, leaving the longitudinal axis free for sample placement.

2.2. Quantification of activity and cross section evaluation

Radioactivities were quantified by gamma spectrometry using an Al-windowed HPGe and MAESTRO software (ORTEC). ¹⁵²Eu check sources were used to calibrate the energy and determine the efficiency of HPGe at ND and UWM. The following function [11]:

$$\ln(\eta(E)) = A + B\ln(E) + C\ln(E)^{2} + D\ln(E)^{3}$$
(1)

Was used to fit efficiency values for gamma emission energies above 240 keV (see Fig. 2). The fit was within $\pm 3\%$ of the data and we observed no improvement in the fit beyond third order

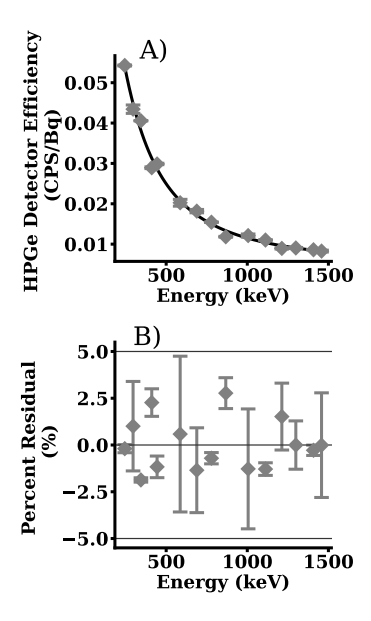


Fig. 2. A) Efficiency calibration of HPGe at UWM with a 152 Eu check source approximately 2 cm away from the face of the detector. The solid line corresponds to the fit presented in equation (1). B) Residuals of the data to the fit. Horizontal delineations at $\pm 5\%$ and 0% are for visual aid.

in $\ln(E)$. Error bars in Fig. 2 correspond to one standard deviation from counting statistics only. All samples assayed at UWM were placed in the same position, approximately 2 cm away from the face of the detector. Samples at ND were placed at various positions to optimize 51 Mn signal-to-noise ratio. The impact of coincidence summing was found to be negligible (see figure S2). The activity of the 152 Eu check source at UWM was ascertained with a 133 Ba check source using the 296 keV and 303 keV emission from 152 Eu and 133 Ba, respectively. All check-sources used are traceable to NIST. Gamma emission intensities and half-lives were all taken from IAEA's nuclear database [12]. HPGe data were cross-referenced between ND and UWM and found to be agreeable within uncertainties. Produced radionuclides relevant to this work are presented in Table 1. The chosen gamma emission of interest was used to tabulate peak area and define the region of interest (ROI).

A Gaussian and cubic polynomial were used to fit the peak ROI using a non-linear least squares optimization to better estimate the background counts within the ROI:

$$Fit = Ne^{\frac{(x-\mu)^2}{2\sigma^2}} + Ax^3 + Bx^2 + Cx + D \tag{2}$$

The number of bins in the ROI was determined by using four standard deviations of the fitted Gaussian and the total background count was determined as the trapezoidal area from the edges of the fitted ROI. The signal of interest was calculated by subtracting the trapezoidal area from the total raw counts in the ROI. Fig. 3 shows sample spectra taken from HPGe with their respective fits

As can be seen from the low signal-to-noise ratio of ⁵¹Mn (Fig. 3A), an appealing alternative for assaying ⁵¹Mn is through its longer-lived ⁵¹Cr decay product (Fig. 3B). Although an accurate measure of ⁵¹Mn from ⁵¹Cr requires a waiting period longer than ten half-lives of ⁵¹Mn (>8 h), it also allows decay of other short-lived radionuclides to reduce background in the ROI. Other

Table 1 Nuclear data of produced radionuclides relevant to this work. Threshold energies were taken from [13]. Radionuclides are not listed if the threshold energy is greater than 18 MeV. 50 V(p, γ) 51 Cr is not listed due to its low significance relative to 51 V(p,n) 51 Cr.

Radionuclide of interest	Half-life	Gamma emission of interest (keV)	Branching ratio (%)	Production pathway; Threshold energy
⁵¹ Cr	27.704d	320.08	9.91	⁵¹ V(p,n) ⁵¹ Cr; 1.565 MeV Decay of ⁵¹ Mn
⁵¹ Mn	46.2 min	749.07	0.265	54 Fe(p, α) 51 Mn; 3.205 MeV 52 Cr(p,2n) 51 Mn; 16.340 MeV
⁵⁶ Co	77.236d	846.77	99.9399	⁵⁶ Fe(p,n) ⁵⁶ Co; 5.445 MeV ⁵⁷ Fe(p,n) ⁵⁶ Co; 13.225 MeV
62 Zn 63 Zn 65 Zn	9.193 h 38.47 min 243.93d	596.56 669.62 1115.54	26.0 8.2 50.04	⁶³ Cu(p,2n) ⁶² Zn; 13.477 MeV ⁶³ Cu(p,n) ⁶³ Zn; 4.215 MeV ⁶⁵ Cu(p,n) ⁶⁵ Zn; 2.167 MeV

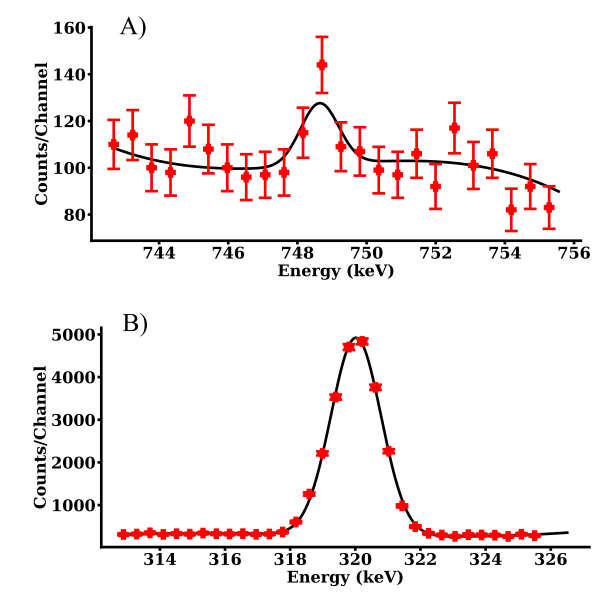


Fig. 3. Sample spectra acquired from HPGe (+ marker) and the fit applied (solid line) for a target receiving $E_{0,p^+}=18$ MeV. A) 749 keV 51 Mn peak acquired at ND, the spectrum was taken 4 h post EOB (end of bombardment) with a live time of 600 s. Only every second data point is plotted. B) 320 keV 51 Cr peak acquired at UWM, the spectrum was taken 21d post EOB with a live time of 9000 s.

advantages from assaying 51 Cr include the ability to transport samples over long transit times, a more precise half-life, better branching ratio and increased detection efficiency. The "critical level" [14] was chosen as the minimum 51 Cr needed to qualitatively distinguish signal from background and was set as $1.65\sigma_{\text{background}}$ in the energy region of the 320 keV peak of interest. This value corresponds to less than 3% of the activity from the 54 Fe target with the smallest amount of 51 Cr. Background from the bare copper backing was investigated and no detectable

⁵¹Cr was observed. Since the bare copper foil did not produce any measurable ⁵¹Cr, and we waited for more than ten half-lives of ⁵¹Mn before assaying ⁵¹Cr, the ⁵¹Cr signal was assumed to be from the complete decay of ⁵¹Mn. The "cross section" of ⁵¹Cr, as obtained from assaying ⁵¹Cr, was thus used as an indirect measurement of ⁵¹Mn.

A radio- and UV-sensitive phosphor screen was exposed to the activated foils to enable visual inspection of the beam profile. A low intensity UV light was shone perpendicularly above the aluminum-mounted targets to develop a registered profile of the rectangular target frame. The exposed screen was readout with PerkinElmer's Cyclone Plus instrument and digitally processed with OptiQuant software. Contour images of the radiosignal were drawn using MATLAB[®]. Radiosignals were not calibrated but were linearly correlated with activity. Experiments with point sources (physical radius < 1 mm) revealed that the true physical distribution was entirely contained within the upper 75% of the max radiosignal. A 20-30% threshold of the max radiosignal was enough to contain >99% of the developed radiosignal within a 9 mm diameter circle. A measured activation profile is shown in Fig. 1C, where radiosignals less than 15% of the maximum have been removed to enhance visibility.

Cross sections for the measurements described above were calculated from the activation equation for thin foils (Eq. (3)). Given the activity at EOB (end of bombardment), assuming the irradiation does not produce a parent of the desired radionuclide, the cross section is:

$$\sigma(E) = \frac{A(T_{\text{EOB}})}{\lambda I_A \left(e^{-\lambda t'} * I(E, t')\right) \mid_{T_{\text{EOB}}}}$$
(3)

Where λ is the decay constant of the radionuclide, $l_{\rm A}$ is the atomic areal density of the target (after correcting for isotopic abundance), I(E,t) is the beam current at a particular energy as a function of time, $T_{\rm EOB}$ is the irradiation time and the convolution, indicated by *, is evaluated at $T_{\rm EOB}$. Less than 1% difference was observed between convolving the exponential decay of ⁵¹Mn with the current signal measured from the chamber and using the average current for all the targets of interest.

The activity at EOB was calculated from the counts registered on the HPGe gamma detector in the following way:

$$A(T_{\text{EOB}}) = \frac{N(E)}{t_{\text{live}}} \frac{t_{\text{real}}}{t_{\text{live}}} \frac{\lambda t_{\text{real}}}{\eta(E) BR(1 - e^{\lambda t_{\text{real}}}) e^{-\lambda T_{\text{elapsed}}}}$$
(4)

Where N(E) is the background-subtracted number of counts at a particular ROI, $t_{\rm real}$ is the real time during counting, $t_{\rm live}$ is the live time during counting, $\eta(E)$ is the calibration efficiency for the HPGe detector at a particular energy, BR is the branching ratio of the gamma emission and $T_{\rm elapsed}$ is the time elapsed since EOB at the start of counting.

2.3. Iron abundance validation

Though ^{55}Co could theoretically be used to analyze ^{56}Fe impurities, production of ^{55}Co from $^{54}\text{Fe}(p,\gamma)^{55}\text{Co}$ is comparable to $^{56}\text{Fe}(p,2n)^{55}\text{Co}$ with a vendor-stated 0.3% ^{56}Fe impurity. At the energies investigated in this paper, production of ^{56}Co is only possible from ^{56}Fe and ^{57}Fe . With $^{57}\text{Fe}(p,2n)^{56}\text{Co}$ cross sections being comparable to $^{56}\text{Fe}(p,n)^{56}\text{Co}$ at $E_{0,p^+}=13\text{-}18$ MeV and negligible below 13 MeV [3], we have assumed the main production pathway of ^{56}Co to be $^{56}\text{Fe}(p,n)^{56}\text{Co}$ due to the low vendor-reported ^{57}Fe impurity in our sample (0.01% ^{57}Fe as compared with 0.3% ^{56}Fe). The presence of ^{56}Co was used to determine potential ^{56}Fe impurities

by comparing the reported cross section values on EXFOR/literature to those obtained from this work. Explicitly, the relative impurity as an isotopic fraction is calculated by:

Impurity ratio =
$$\frac{\sigma_{\text{this work}}}{\sigma_{\text{literature}}}$$
 (5)

Where $\sigma_{this\ work}$ refers to the cross section of 56 Co found from this work, assuming that the entire sample was made of 56 Fe, and $\sigma_{literature}$ is the reported 56 Fe(p,n) 56 Co cross section. nat Fe(p,x) 56 Co data from [15] and [16] were used as $\sigma_{literature}$ after correcting for the 91.75% 56 Fe abundance. The determined 56 Fe impurity ranged from 0.30-0.47% (see figure S1A), which is in agreement with isotopic impurity values in the vendor-reported 54 Fe COA (certificate of analysis). As such, 99.7% 54 Fe was used to correct the plated iron mass.

Once all the data were acquired, samples were dissolved in 1.8 mL 6 M HCl and 0.2 mL 30% H₂O₂. A 50 µL aliquot from the homogenous sample solution was added to 9.950 mL of 0.1 M HCl. The diluted samples were then analyzed on a Microwave-Plasma Atomic Emission Spectroscopy instrument (4210MP-AES, Agilent Technologies) to quantify iron in the target. Sets of four standard concentrations ranging from 5 ppm-100 ppm of copper and iron were used for linear calibration curves ($R^2 > 0.999$). To reduce systemic errors from MP-AES, the mass ratio of copper to iron was used to compare measurements from the digital scale and MP-AES. Given that the relative uncertainty of copper's mass from the digital scale is <2%, the absolute mass of iron was taken to be the mass of copper from the digital scale divided by the mass ratio of copper to iron as obtained from MP-AES. Copper was analyzed using wavelengths of 324.754 nm, 327.395 nm and 510.554 nm, and iron was analyzed using wavelengths of 371.993 nm and 438.354 nm. The selected wavelengths were chosen to maximize the intensity, provide redundancy and avoid overlap with other elements from MP-AES. The system was operated at a constant, stable temperature throughout each independent measurement (N = 3, each performed in triplicate). The final mass of ⁵⁴Fe used in computing the cross section was taken to be the weighted (reciprocal variance) average of measurements from the digital scale and MP-AES. All mass measurements from the digital scale agreed with MP-AES within uncertainty except for target 5, where the weighted average mass differed by +7% (.3 mg) from the digital scale (see figure S1B). The dissolved iron was then separated from copper (via precipitation of copper oxalate) and recycled for ⁵⁴Fe target fabrication.

2.4. Uncertainties

Uncertainties in this work correspond to one standard deviation about the mean reported value. The Poisson heuristic was applied to determine the uncertainty from registered counts on HPGe. Uncertainties of 6% and 5% were assumed for HPGe efficiency calibration and beam current registered from the electrically isolated chamber, respectively. The efficiency calibration uncertainty accounts for uncertainties in the $^{152}\rm{Eu}$ activity (4%), the fit (3%) and the slight differences between target geometry and position from HPGe (3%). Due to relatively low power transfer to the targets, recoil losses were considered negligible from beam current measurements. Since the desired $E_{0,p+}$ was well within 100 keV of the setpoint, energy uncertainties are simply reported as ± 0.1 MeV to include stopping power effects throughout the $^{54}\rm{Fe}$ layer. Uncertainties from MP-AES were evaluated experimentally by having N = 3 repeated measurements of known standard concentrations and samples (each performed in triplicate); uncertainties, including calibration, were within 8%. The $^{51}\rm{Cr}$ activity, calculated from HPGe spectra at ND and UWM after decay correcting to EOB, were combined into a weighted average (reciprocal variance of activity at

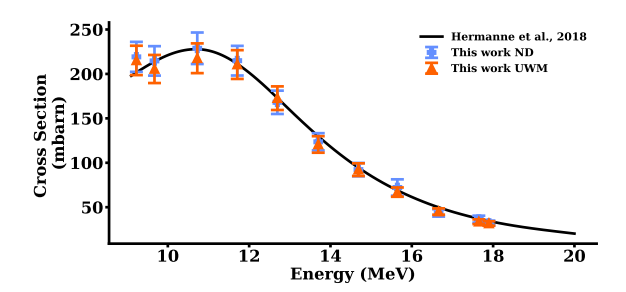


Fig. 4. Comparison of the cross section values for nat Cu(p,x) 65 Zn from this work to IAEA's recommended cross section values [17].

EOB) to reduce uncertainties from HPGe quantification. The final absolute uncertainty is the result of summing the appropriate relative errors in quadrature and scaling with the cross section.

3. Results and discussion

3.1. IAEA $^{nat}Cu(p,x)^{65}Zn$ monitor reaction

The measured ⁶⁵Zn cross sections agree within uncertainty to IAEA's recommended values [17] (see Fig. 4). The 1115 keV gamma emission of ⁶⁵Zn was used to tabulate the peak area.

3.2. ${}^{54}Fe(p,\alpha){}^{51}Mn$ excitation function

The resulting excitation function is plotted in Fig. 5 against calculated values from TENDL-2019 and experimental data from Levkovski [3]. Explicit values of cross section from this work can be found in Table 2. Although the directly obtained ⁵¹Mn cross sections had high uncertainties and deviations from reported values, they still agree with cross sections calculated from ⁵¹Cr quantification. The 749 keV gamma emission of ⁵¹Mn and 320 keV gamma emission of ⁵¹Cr were used to tabulate their respective peak areas. Data below the limit of detection (as described earlier) are labeled as 'N/A'. Most of our data agrees with [3] within uncertainties, and especially so if an approximate 10% reduction is applied for reported cross sections above 15 MeV. This potential systematic difference is corroborated by reports that [3] may have slightly overestimated values of its monitor reaction [6]. Theoretical predictions from TENDL-2019 were generally lower than Levkovski's experimental results and in better agreement with this work, but the shape of the excitation function is consistent between all sources.

3.3. Optimal ⁵¹Mn production parameters

The "optimal" irradiation time:

$$t_{\text{optimal}} = \operatorname{argmax}_{t}(\frac{A_{51}_{\text{Mn}}}{A_{51}_{\text{Cr}}}A_{51}_{\text{Mn}})$$
(6)

was found to be approximately 1.4 h and results in roughly 72% of the saturated yield. In equation (6), $A_{^{51}Mn}$ is the activity of ^{51}Mn at EOB and $A_{^{51}Cr}$ is the total activity of ^{51}Cr once ^{51}Mn has fully decayed. $t_{optimal}$ can be interpreted as the irradiation time that reduces the relative amount of ^{51}Cr produced while simultaneously maximizing $A_{^{51}Mn}$. Reducing the irradiation time reduces

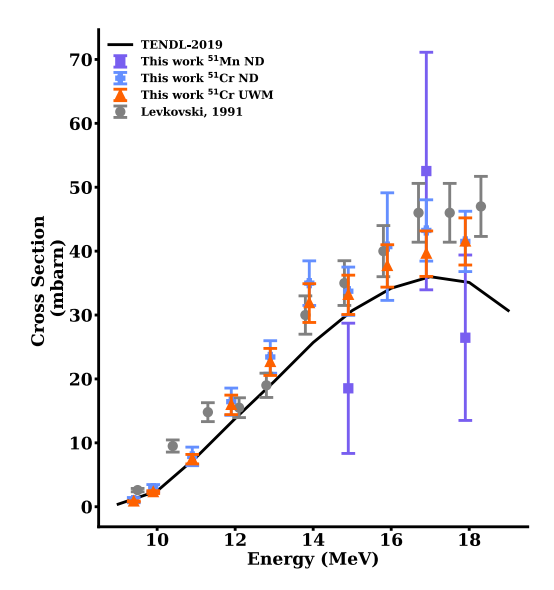


Fig. 5. Excitation function of 54 Fe(p, α) 51 Mn from this work compared with Levkovski's data [3]. Calculated values from TENDL-2019 are also presented to show the predicted general trend.

Table 2 Measured 54 Fe(p, α) 51 Mn cross sections from this work using the two techniques described previously, and with an intercomparison between UWM and ND. The presence of 51 Cr was only possible due to the decay of 51 Mn and not from proton induced reactions in our sample. Cross sections measured using 51 Cr are labeled as such. Cross sections computed using a weighted average of 51 Cr activity at ND and UWM are also reported.

-		•	_	
Midpoint energy ±0.1 [MeV]	σ [mb] *from ⁵¹ Cr at UWM	σ [mb] *from ⁵¹ Cr at ND	σ [mb] *from ⁵¹ Mn at ND	σ [mb] *Weighted average of ⁵¹ Cr from UWM and ND
17.9	41.5±3.7	41.5±4.7	26.4±12.9	41.5±3.1
16.9	39.6 ± 3.6	43.2 ± 4.8	52.5 ± 18.6	40.5 ± 3.7
15.9	37.7 ± 3.3	40.7 ± 8.4	N/A	37.8 ± 2.9
14.9	33.2 ± 3.1	33.7 ± 3.8	18.5 ± 10.2	33.4 ± 2.5
13.9	31.9 ± 3.0	35.0 ± 3.5	N/A	33.1 ± 3.2
12.9	22.7 ± 2.1	23.4 ± 2.5	N/A	22.9 ± 1.8
11.9	15.9 ± 1.5	16.4 ± 2.1	N/A	16.0 ± 1.2
10.9	7.44 ± 0.74	7.88 ± 1.45	N/A	7.49 ± 0.59
9.9	2.29 ± 0.22	2.90 ± 0.56	N/A	2.33 ± 0.28
9.4	0.83 ± 0.09	1.03 ± 0.41	N/A	$0.84 {\pm} 0.08$

the total amount of any radionuclides produced but one advantage is that it also reduces the relative amounts of ⁵⁶Co and ⁵⁵Co, a potential source of concern in clinical productions of ⁵¹Mn. The optimal areal density of the target, with respect to cost, was found to be 181 mg/cm² at 16.1 MeV and corresponds to about 89% of the thick (270 mg/cm²) target yield, when all other parameters are considered equal. Increasing areal density increases the relative amounts of ⁵⁶Co and ⁵⁵Co since their relative cross sections are heavily favored at lower energies. Despite this potential concern, there exists published method [7,18] to separate manganese from cobalt.

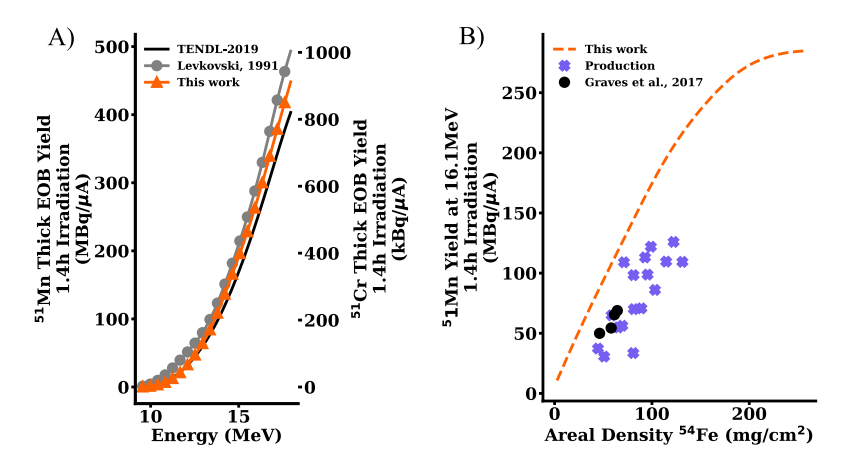


Fig. 6. A) Thick target yield at the optimal irradiation time of 83.9 minutes using the excitation function measured from this work. The stopping power of protons in iron was taken from SRIM [19]. B) Comparing the results from this work to that of various ⁵¹Mn productions at UWM, including results reported by [1].

Using the optimal irradiation time and the data obtained from this work, a thick target yield [20] over the energies investigated is presented in Fig. 6A. A cubic spline interpolation was used to generate finer cross section and stopping power values for integration. A 16.1 MeV, 30 µA proton beam impinging on a target with areal density of 181 mg/cm² for 1.4 h will form 7.62 GBq of ⁵¹Mn at EOB. Yields from ⁵¹Mn production at UWM with a PETtraceTM cyclotron (GE Healthcare) are compared to the results of this work (Fig. 6B), where the irradiation time has been normalized to 1.4 h. An average beam current correction factor of about 2 (varies for each irradiation) was determined from irradiating radiochromic film and analyzing the resulting beam geometry relative to a 1 cm diameter target [21]. The calculated yields obtained from this work agree to ⁵¹Mn productions at UWM using 1 cm diameter targets with this correction factor.

Nevertheless, our results show that using 54 Fe targets with an areal density of 100 mg/cm^2 can yield clinically relevant quantities of 51 Mn at EOB (>3.5 GBq) with just $40 \mu Ah$ ($40 \mu A$, 1 h) using the PETtraceTM. The previous statement assumes that personnel handling 51 Mn will achieve an end of chemistry yield >740 MBq, which has already been accomplished by [1] if scaled by the EOB yield.

4. Conclusion

The results presented in this article correspond to the work of Levkovski within uncertainty. Gamma spectrometric assays from UWM were consistent with results from ND, and 65 Zn cross section data from this work agrees within uncertainties to IAEA's recommended dataset. Electrodeposition of 54 Fe onto nat Cu foils was instrumental in fabricating thin-foil targets. Thick target yields at the optimal time point and optimal target areal densities were also presented using the data acquired from this work and compared to production of 51 Mn at UWM, with results agreeing after correcting for beam-target incidence. To our knowledge, this work is the first investigation of 54 Fe(p, α) 51 Mn excitation function presented in a peer reviewed publication. We hope these results enable optimization of routine 51 Mn production using the globally distributed constellation of small cyclotrons and accelerators.

CRediT authorship contribution statement

Wilson Lin: Formal analysis, Investigation, Methodology, Software, Validation, Visualization, Writing – original draft, Writing – review & editing. John T. Wilkinson: Investigation, Methodology, Visualization, Writing – review & editing. Kendall E. Barrett: Investigation, Visualization, Writing – review & editing. Todd E. Barnhart: Methodology, Resources, Supervision, Writing – review & editing. Matthew Gott: Investigation, Methodology, Resources, Writing – review & editing. Kaelyn V. Becker: Software, Writing – review & editing. Adam M. Clark: Methodology, Writing – review & editing. Anthony Miller: Investigation, Writing – review & editing. Gunnar Brown: Writing – review & editing. Molly DeLuca: Writing – review & editing. Robert Bartsch: Writing – review & editing. Graham F. Peaslee: Funding acquisition, Methodology, Project administration, Resources, Supervision, Writing – review & editing. Jonathan W. Engle: Conceptualization, Funding acquisition, Methodology, Project administration, Resources, Supervision, Visualization, Writing – review & editing.

Declaration of competing interest

The authors declare that they have no known competing financial interests or personal relationships that could have appeared to influence the work reported in this paper.

Acknowledgement

This work would not have been possible without the support from the Institute for Structure and Nuclear Astrophysics group and the associated Nuclear Science Laboratory at the University of Notre Dame. The authors would like to thank Edward Stech of ND for his technical support in operating the accelerator as well as logistics associated with radiation safety. Jonathan W. Engle and Kaelyn V. Becker are grateful for support from the Department of Energy's (DOE's) Office of Science Isotope Program (awards DE-SC0020417), and Jonathan W. Engle and Wilson Lin are grateful for support from NIH/NCI award P01-CA250972. Adam M. Clark is grateful for the support from the NSF under grant No. PHY-2011890 as well as the U.S. Nuclear Regulatory Commission award 31310019M0037.

Appendix A. Supplementary material

Supplementary material related to this article can be found online at https://doi.org/10.1016/j.nuclphysa.2022.122424.

References

- S.A. Graves, R. Hernandez, H.F. Valdovinos, P.A. Ellison, J.W. Engle, T.E. Barnhart, et al., Preparation and in vivo characterization of ⁵¹MnCl₂ as PET tracer of Ca2⁺ channel-mediated transport, Sci. Rep. 7 (2017) 3033, https:// doi.org/10.1038/s41598-017-03202-0.
- [2] R. Hernandez, S.A. Graves, T. Gregg, H.R. VanDeusen, R.J. Fenske, H.N. Wienkes, et al., Radiomanganese PET detects changes in functional β-cell mass in mouse models of diabetes, Diabetes 66 (2017) 2163–2174, https://doi.org/10.2337/db16-1285.
- [3] V.N. Levkovski, Cross-Section of Medium Mass Nuclide Activation (A = 40–100) by Medium Energy Protons and Alpha Particles, Inter-Vesi, Moscow, 1991.

- [4] A.T.J. Klein, F. Rösch, S.M. Qaim, Investigation of ⁵⁰Cr(d,n)⁵¹Mn and ^{nat}Cr(p,x)⁵¹Mn processes with respect to the production of the positron emitter ⁵1Mn, Radiochim. Acta 88 (2000) 253–264, https://doi.org/10.1524/ract.2000. 88.5.253.
- [5] M. Cogneau, L. Gilly, J. Cara, Absolute cross sections and excitation functions for deuteron induced reactions on chromium between 2 and 12 MeV, Nucl. Phys. 79 (1966) 203–208, https://doi.org/10.1016/0029-5582(66)90403-2.
- [6] IAEA, Charged particle cross-section database for medical radioisotope production: diagnostic radioisotopes and monitor reactions 2001, https://www-pub.iaea.org/MTCD/Publications/PDF/te_1211_prn.pdf (Accessed 27 August 2021).
- [7] H.F. Valdovinos, R. Hernandez, S. Graves, P.A. Ellison, T.E. Barnhart, C.P. Theuer, et al., Cyclotron production and radiochemical separation of ⁵⁵Co and ^{58m}Co from ⁵⁴Fe, ⁵⁸Ni and ⁵⁷Fe targets, Appl. Radiat. Isot. 130 (2017) 90–101, https://doi.org/10.1016/j.apradiso.2017.09.005.
- [8] S.R. McGuinness, A Heavy-Ion Approach to Radiomedicine, University of Notre Dame, 2021.
- [9] S.R. McGuinness, J.T. Wilkinson, G.F. Peaslee, Heavy-ion production of ⁷⁷Br and ⁷⁶Br, Sci. Rep. 11 (2021) 15749, https://doi.org/10.1038/s41598-021-94922-x.
- [10] M. Skulski, T. Anderson, L. Callahan, A.M. Clark, A.D. Nelson, D. Robertson, et al., Recent developments in the AMS system at the nuclear science laboratory: impacts on radionuclide sensitivities and current capabilities, Nucl. Instrum. Methods Phys. Res., Sect. B, Beam Interact. Mater. Atoms 488 (2021) 30–36, https://doi.org/10.1016/j. nimb.2020.12.009.
- [11] G.L. Molnár, Zs. Révay, T. Belgya, Wide energy range efficiency calibration method for Ge detectors, Nucl. Instrum. Methods Phys. Res., Sect. A, Accel. Spectrom. Detect. Assoc. Equip. 489 (2002) 140–159, https://doi.org/10.1016/S0168-9002(02)00902-6.
- [12] From ENSDF database as of August 28, Version available at http://www.nndc.bnl.gov/ensarchivals/, 2021.
- [13] B. Pritychenko, A. Sonzogni, Q-value Calculator (QCalc) n.d., https://www.nndc.bnl.gov/qcalc/ (Accessed 30 August 2021).
- [14] L.A. Currie, Limits for qualitative detection and quantitative determination. Application to radiochemistry, Anal. Chem. 40 (1968) 586–593, https://doi.org/10.1021/ac60259a007.
- [15] S. Takács, L. Vasváry, F. Tárkányi, Remeasurement and compilation of excitation function of proton induced reactions on iron for activation techniques, Nucl. Instrum. Methods Phys. Res., Sect. B, Beam Interact. Mater. Atoms 89 (1994) 88–94, https://doi.org/10.1016/0168-583X(94)95152-7.
- [16] M. Al-Abyad, M.N.H. Comsan, S.M. Qaim, Excitation functions of proton-induced reactions on ^{nat}Fe and enriched ⁵⁷Fe with particular reference to the production of ⁵⁷Co, Appl. Radiat. Isot. 67 (2009) 122–128, https://doi.org/10.1016/j.apradiso.2008.07.006.
- [17] A. Hermanne, A.V. Ignatyuk, R. Capote, B.V. Carlson, J.W. Engle, M.A. Kellett, et al., Reference cross sections for charged-particle monitor reactions, Nucl. Data Sheets 148 (2018) 338–382, https://doi.org/10.1016/j.nds.2018.02. 009
- [18] K.E. Barrett, E. Aluicio-Sarduy, A.P. Olson, C.J. Kutyreff, P.A. Ellison, T.E. Barnhart, et al., Radiochemical isolation method for the production of ^{52g}Mn from ^{nat}Cr for accelerator targets, Appl. Radiat. Isot. 146 (2019) 99–103, https://doi.org/10.1016/j.apradiso.2019.01.025.
- [19] J.F. Ziegler, M.D. Ziegler, Biersack J.P., SRIM the stopping and range of ions in matter (2010), Nucl. Instrum. Methods Phys. Res., Sect. B 268 (2010) 1818–1823, https://doi.org/10.1016/j.nimb.2010.02.091.
- [20] Definitions of radioisotope thick target yields n.d., https://www.degruyter.com/document/doi/10.1515/ract-2013-2234/html (Accessed 28 August 2021).
- [21] H. Valdovinos, R. Hernandez, S. Goel, S. Graves, T. Barnhart, W. Cai, et al., Cyclotron production of ^{58m}Co for Auger electron-based targeted radioimmunotherapy and PET imaging post-therapy with the daughter ^{58g}Co, J. Nucl. Med. 57 (2016) 332–332.